aerospace

MDPI

Article

Frequency-Dependent Rotordynamic Coefficients of Supercritical CO_2 Labyrinth Seals Considering Real Gas Effects

Qidong Zhang [1], Wanfu Zhang [1], Qianlei Gu [1,*], Weirong Wu [1], Chun Li [1], Weipao Miao [1], Minnan Yue [1] and Jiangang Yang [2]

[1] School of Energy and Power Engineering, University of Shanghai for Science and Technology, No. 516, Jungong Road, Shanghai 200093, China; qidongzhang_usst@163.com (Q.Z.); wfzhang@usst.edu.cn (W.Z.); weirongwu037@163.com (W.W.); lichun_usst@163.com (C.L.); mwpusst@usst.edu.cn (W.M.); windgroup@yeah.net (M.Y.)

[2] School of Energy and Environment, Southeast University, No. 2, Sipailou, Nanjing 210096, China; jgyang@seu.edu.cn

* Correspondence: qianleigu95@usst.edu.cn

Abstract

The Brayton cycle based on supercritical carbon dioxide (S-CO_2) is widely used in turbomachinery. In this paper, the rotordynamic coefficients are systematically investigated for the labyrinth seal working with S-CO_2 based on NIST REFPROP database. A three-dimensional numerical model of the labyrinth seal was developed using computational fluid dynamics (CFD). The rotordynamic characteristics of the labyrinth seal for different boundary conditions and various geometries were studied over a wide frequency range of 20–260 Hz. Results show that the direct complex stiffness coefficient exhibits strong frequency dependence in the low-frequency region, while the cross-coupled complex stiffness coefficient and average direct damping coefficient exhibit relatively slight frequency dependency. The effective damping coefficient increases with the increasing inlet pressure, rotational speed, blade quantities, and decreasing inlet temperature. The effective damping coefficient has a strong frequency dependency at low whirling frequencies less than 80 Hz and increases slightly with the decreasing sealing clearance. At high whirling frequencies above 80 Hz, the effective damping coefficient increases with the increasing sealing clearance. The effective damping coefficient of the labyrinth seal with S-CO_2 is about 167~202% of that with air modeled as an ideal gas, indicating a more favorable contribution of the seal to rotordynamic stability. The frequency-dependent trends of the rotordynamic coefficients under real gas conditions differ significantly from those under ideal gas conditions, highlighting the importance of real gas effects for accurately predicting the rotordynamic performance and stability of S-CO_2 labyrinth seals.

Keywords: labyrinth seals; supercritical carbon dioxide; computational fluid dynamics; rotordynamic characteristics; effective damping coefficient; stability

Check for updates

Academic Editor: Erinc Erdem

Received: 22 September 2026
Revised: 28 October 2026
Accepted: 30 October 2026
Published: 31 October 2026

Copyright: © 2026 by the authors. Licensee MDPI, Basel, Switzerland. This article is an open access article distributed under the terms and conditions of the Creative Commons Attribution (CC BY) license.

1. Introduction

Recently, efficient energy utilization and environmental protection have become increasingly prominent worldwide. Developing novel energy conversion systems that simultaneously achieve high efficiency, compact layout and operational safety has emerged as a critical research direction in the field of advanced energy technologies [1,2]. Supercritical carbon dioxide (S-CO_2) possesses superior thermophysical characteristics, including high fluid density, low viscosity, low compression power consumption and excellent heat transfer

performance [3,4]. Accordingly, turbomachinery based on the S-CO_2 Brayton cycle has attracted extensive research attention in recent decades [5–7].

Seals are indispensable core components of turbomachinery, which serve to restrain working fluid leakage and maintain overall cycle efficiency. Meanwhile, fluid forces generated within the internal flow field of seals fundamentally determine the rotordynamic stability of rotor systems [8,9]. For turbine seals operating with conventional working fluids, such as air and water vapor, numerous systematic investigations have been implemented to clarify the seal impacts on unit efficiency and rotordynamic performance, and the corresponding theoretical systems have been well established [10–12]. Nevertheless, unlike conventional working fluids, the thermophysical properties of S-CO_2 near its critical point, including density, viscosity, specific heat, speed of sound, enthalpy and entropy, exhibit strongly nonlinear variations with pressure and temperature [13]. Such distinctive physical properties make the traditional seal design methodologies established for conventional fluids inapplicable to S-CO_2 turbomachinery [14,15].

To clarify the discrepancies in leakage behaviors and rotordynamic characteristics between S-CO_2 and conventional working fluids, which would guide the engineering design of S-CO_2 seals, many researchers have conducted in-depth studies on S-CO_2 seal systems. Yin et al. [16] investigated staggered labyrinth seals for S-CO_2, and demonstrated that the real gas effect can remarkably alter seal stiffness and damping coefficients, thereby deteriorating the dynamic stability of rotor systems. A series of subsequent studies by Xu et al. [17], Odabaee et al. [18], Zeng et al. [19] and Xiong et al. [20] further confirmed that the real gas effect of S-CO_2 modifies the dynamic mechanical properties of seal gas films. And the real gas effect renders the entire system highly sensitive to local thermal operating conditions. In particular, Si et al. [21] pointed out that the nonlinear thermophysical properties in the vicinity of the critical point amplify the influences of the real gas effect on seal dynamic parameters. Consequently, S-CO_2 presents distinct leakage characteristics and fluid excitation effects under variable operating conditions compared with conventional working fluids. Lu et al. [22] reported that operational fluctuations in the S-CO_2 recompression cycle couple with the real gas effect, which significantly exacerbates shaft seal leakage and reduces the operational safety margin of power units. Bidkar et al. [23] observed pronounced viscous shear and windage heating phenomena of S-CO_2 in hydrodynamic face seals. In research on spiral-groove dry gas seals, Yuan et al. [24] further concluded that the S-CO_2 real gas effect changes the hydrodynamic pressure generation mechanism of face gas films, leading to an essential shift in the correlation between seal opening force and leakage rate.

Aiming at high-speed operating conditions, Zhang et al. [25,26] explored scallop damper seals and found that the nonlinear thermophysical properties of S-CO_2 at high rotating speeds intensify gap vortex shedding and turbulent dissipation. Additionally, the flow-induced vibration of such seals is extremely sensitive to geometric dimensions. This rule is also valid for other seals. Numerical simulations by Zhu et al. [27] verified that the influence laws of geometric parameters on the leakage performance of stepped staggered labyrinth seals using real S-CO_2 differ fundamentally from those of conventional fluids. Specifically, the regulation effects of structural modifications, including radial clearance and length-to-height ratio, on leakage are greatly amplified by the real gas effect. Li et al. [28] found that different from the linear variation in leakage for conventional fluids, the real gas effect of S-CO_2 induces a nonlinear growth of leakage with changing structural parameters. Meanwhile, the overall seal stiffness increases, whereas the effective damping decreases obviously.

The above studies have laid a solid foundation for understanding the differences between S-CO_2 seals and conventional fluid seals. However, most existing works only focus on leakage and rotordynamic performance under fixed operating conditions, and

the variation in rotordynamic characteristics with whirl frequency is rarely addressed. In practice, S-CO_2 turbomachinery generally operates at high rotating speeds, with a maximum rotational speed up to 20,000 r/min [29,30]. It means that S-CO_2 Brayton cycle units face an extremely wide range of whirl frequencies during actual operation. Previous investigations on air, water vapor and other gaseous working fluids have fully proven that the rotordynamic coefficients of seals possess strong frequency dependence [31,32]. For S-CO_2 seals, this frequency dependence becomes more complicated because the thermophysical properties vary strongly with pressure and temperature, which may alter not only the magnitude but also the frequency-dependent trends of the rotordynamic coefficients. As a result, frequency-dependent coefficients obtained under ideal gas assumptions may not be directly applicable to S-CO_2 seals. Despite this, systematic research on the frequency-dependent rotordynamic coefficients and system stability of S-CO_2 seals under wide-range whirl conditions is still insufficient.

To explore the actual performance and stable operation of S-CO_2 seal systems over a broad frequency range, this study focuses on the frequency-dependent rotordynamic characteristics of labyrinth seals under wide-range whirl conditions and their influence on seal system stability. A three-dimensional CFD model is established for the seal by incorporating the NIST REFPROP database to account for real gas thermophysical effects. The classical perturbation theory and transient flow simulation are adopted to extract the rotordynamic coefficients over a wide frequency range of 20–260 Hz. The effects of inlet pressure, inlet temperature, rotational speed, blade number, and radial clearance are then analyzed, and a comparison between S-CO_2 and air is conducted. By clarifying the role of real gas effects in the frequency-dependent rotordynamic coefficients, this work provides a reliable basis for the stability design and engineering optimization of S-CO_2 labyrinth seals beyond air-based approximations.

2. Numerical Methods

2.1. Seal Configuration

In this paper, the numerical model is based on the labyrinth seal in author's laboratory. Figure 1 gives the cross section of the labyrinth seal, which includes 10 blades with a radial clearance of 0.20 mm, seal length of 35.7 mm. In order to study the effect of the blade quantities and radial clearances on the seal dynamic characteristics, the labyrinth seal with four types of blades (4, 6, 8, 10 blades) and five clearances (0.16 mm, 0.20 mm, 0.24 mm, 0.28 mm, 0.32 mm) are also employed in the numerical simulation. Table 1 gives the detailed dimensions.

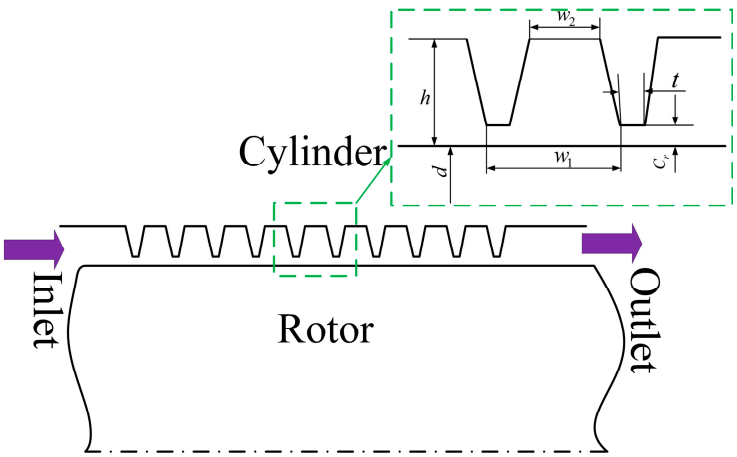


Figure 1. Two-dimensional geometry model of the labyrinth seal.

Table 1. Seal dimensions.

Parameter	Value
Seal length l/mm	12.9, 20.5, 28.1, 35.7
Seal inner diameter d/mm	60
Radial clearance C_r/mm	0.16, 0.20, 0.24, 0.28, 0.32
Number of blades	4, 6, 8, 10
Cavity width w_1/mm	3.8
Cavity depth h/mm	3.5
Blade thickness t/mm	0.25
Blade space width w_2/mm	2.3

2.2. Identification Method for Rotordynamic Coefficients

A method for identifying seal dynamic characteristics based on infinitesimal perturbation theory [33] is applied to solve the rotordynamic characteristics of arbitrary elliptical trajectories and eccentric positions under actual conditions.

Figure 2 presents a two-dimensional schematic of the rotordynamic model. The rotor is assumed to whirl along an elliptical orbit at an arbitrary eccentric position. In the system, O is the housing center, $O_1{}'$ is the rotor center, O_1 is the whirling center, and ω is the rotational speed of the rotor. The origins of the coordinate systems: (x, y) and (η, ξ) are, respectively, O and O_1, rotating the coordinate system of (η, ξ) counterclockwise by θ. Then the e-axis and α-axis coincide with the major and minor axis of the elliptical orbit, and coordinate system (e, α) is established.

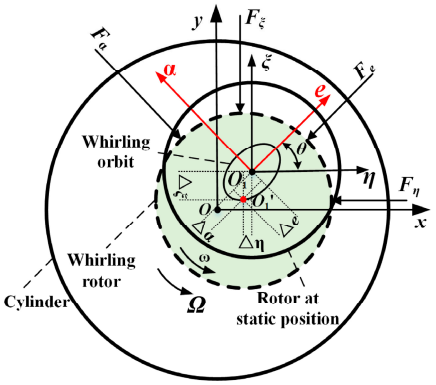


Figure 2. Rotordynamic model for annular seals.

For a rotor undergoing elliptical whirling at angular frequency Ω_i $(i = 1, 2, 3, ..., n)$, the orbit in the (x, y) coordinate system is expressed as:

$$\begin{cases} x = a \cdot \cos(\Omega_i t) \cos\theta - b \cdot \sin(\Omega_i t) \sin\theta + x_0 \\ y = a \cdot \cos(\Omega_i t) \sin\theta + b \cdot \sin(\Omega_i t) \cos\theta + y_0 \end{cases} \quad (1)$$

where θ is the inclination angle of the elliptical orbit, ranging from 0 to 360 deg; a and b are the semi-major and semi-minor axes, respectively; and x_0 and y_0 are the coordinates of the orbit center in the (x, y) coordinate system.

In the (e, α) coordinate system, the elliptical orbit is expressed as:

$$\begin{cases} e = a \cdot \cos(\Omega_i t) \\ \alpha = b \cdot \sin(\Omega_i t) \end{cases} \quad (2)$$

The corresponding rotor whirling velocities are:

$$\begin{cases} \dot{e} = -a \cdot \Omega_i \cdot \sin(\Omega_i t) \\ \dot{\alpha} = b \cdot \Omega_i \cdot \cos(\Omega_i t) \end{cases} \quad (3)$$

The corresponding rotor whirling accelerations are:

$$\begin{cases} \ddot{e} = -a \cdot \Omega_i^2 \cdot \cos(\Omega_i t) \\ \ddot{\alpha} = -b \cdot \Omega_i^2 \cdot \sin(\Omega_i t) \end{cases} \tag{4}$$

A coordinate system is established with its origin at O_1. For a small whirling orbit of the rotor, when we consider the mass inertia force, the dynamic model can be simplified as following:

$$-\begin{Bmatrix} \Delta F_e \\ \Delta F_\alpha \end{Bmatrix} = \begin{bmatrix} K_{ee} & K_{e\alpha} \\ K_{\alpha e} & K_{\alpha\alpha} \end{bmatrix} \begin{Bmatrix} e \\ \alpha \end{Bmatrix} + \begin{bmatrix} C_{ee} & C_{e\alpha} \\ C_{\alpha e} & C_{\alpha\alpha} \end{bmatrix} \begin{Bmatrix} \dot{e} \\ \dot{\alpha} \end{Bmatrix} + \begin{bmatrix} M_{ee} & M_{e\alpha} \\ M_{\alpha e} & M_{\alpha\alpha} \end{bmatrix} \begin{Bmatrix} \ddot{e} \\ \ddot{\alpha} \end{Bmatrix} \tag{5}$$

$$-\begin{Bmatrix} \Delta F_e \\ \Delta F_\alpha \end{Bmatrix} = \begin{bmatrix} K_{ee} - \Omega^2 M_{ee} & K_{e\alpha} - \Omega^2 M_{e\alpha} \\ K_{\alpha e} - \Omega^2 M_{\alpha e} & K_{\alpha\alpha} - \Omega^2 M_{\alpha\alpha} \end{bmatrix} \begin{Bmatrix} e \\ \alpha \end{Bmatrix} + \begin{bmatrix} C_{ee} & C_{e\alpha} \\ C_{\alpha e} & C_{\alpha\alpha} \end{bmatrix} \begin{Bmatrix} \dot{e} \\ \dot{\alpha} \end{Bmatrix} \tag{6}$$

where $\Delta F_e = F_e - F_{e_0}$, $\Delta F_\alpha = F_\alpha - F_{\alpha_0}$. (e, α), $(\dot{e}, \dot{\alpha})$ and $(\ddot{e}, \ddot{\alpha})$ are rotor displacements, velocities and acceleration in the e and α directions, respectively. (F_e, F_α) and (F_{e_0}, F_{α_0}) are the seal reaction forces in dynamic and static position. $(K_{ee}, K_{e\alpha}, K_{\alpha e}, K_{\alpha\alpha})$, $(C_{ee}, C_{e\alpha}, C_{\alpha e}, C_{\alpha\alpha})$, $(M_{ee}, M_{e\alpha}, M_{\alpha e}, M_{\alpha\alpha})$ are the stiffness, damping and mass inertia coefficients.

Substituting Equations (2) and (3) into Equation (6) yields:

$$\begin{cases} -\Delta F_e = & a \cdot \left(K_{ee} - \Omega^2 M_{ee}\right) \cos(\Omega t) + b \cdot \left(K_{e\alpha} - \Omega^2 M_{e\alpha}\right) \sin(\Omega t) \\ & -a \cdot C_{ee} \Omega \sin(\Omega t) + b \cdot C_{e\alpha} \Omega \cos(\Omega t) \\ -\Delta F_\alpha = & a \cdot \left(K_{\alpha e} - \Omega^2 M_{\alpha e}\right) \cos(\Omega t) + b \cdot \left(K_{\alpha\alpha} - \Omega^2 M_{\alpha\alpha}\right) \sin(\Omega t) \\ & -a \cdot C_{\alpha e} \Omega \sin(\Omega t) + b \cdot C_{\alpha\alpha} \Omega \cos(\Omega t) \end{cases} \tag{7}$$

The fluid forces acting on the rotor at each whirl angular frequency Ω_i (i = 1, 2, 3, ..., n) are obtained from transient simulations. Figure 3 shows the variation in the seal reaction force with whirling frequencies.

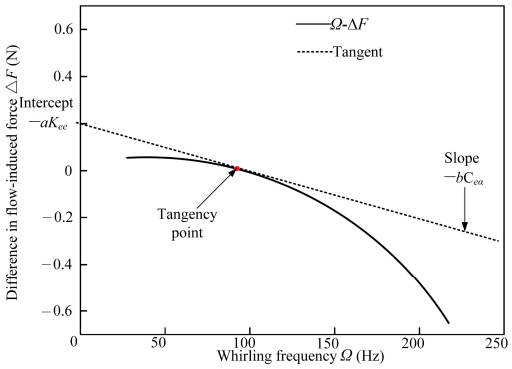


Figure 3. Variation in flow-induced force difference with whirling frequency.

Substituting the forces acting on the rotor within the seal, $\Delta F_e|_{t=0,\Omega=\Omega_i}$ at Ω_i and $\Delta F_e|_{t=0,\Omega=\Omega_i+\Delta\Omega}$ at $\Omega_i+\Delta\Omega$, into Equation (7) yields:

$$\Delta F_e\big|_{t=0,\Omega=\Omega_i} = -a \cdot \left(K_{ee} - \Omega_i^2 M_{ee}\right) - b \cdot C_{e\alpha} \Omega_i \tag{8}$$

$$\Delta F_e\big|_{t=0,\Omega=\Omega_i+\Delta\Omega} = -a \cdot \left[K_{ee} - (\Omega_i + \Delta\Omega)^2 M_{ee}\right] - b \cdot C_{e\alpha} (\Omega_i + \Delta\Omega) \tag{9}$$

Taking the limit as $\Delta\Omega \to 0$ yields:

$$\lim_{\Delta\Omega \to 0} \frac{\Delta F_e\big|_{t=0,\Omega=\Omega_i+\Delta\Omega} - \Delta F_e\big|_{t=0,\Omega=\Omega_i}}{\Delta\Omega} = -b \cdot C_{e\alpha} \tag{10}$$

Thus, the tangent slope at any point on the curve is $-bC_{e\alpha}$ from which the cross-coupled damping coefficient $C_{e\alpha}$ at the corresponding whirl angular frequency is obtained. The tangent intercept on the ordinate is the constant term $-a \cdot (K_{ee} - \Omega^2 M_{ee})$ in Equation (8), from which the combined stiffness–inertia term $K_{ee} - \Omega^2 M_{ee}$ is determined. Similarly, the rotordynamic coefficients at different whirl angular frequencies can be obtained by evaluating the fluid forces at $t = 0$ and $t = \mathrm{T}/4$ where T is the whirling period. For any whirling frequency Ω_i, when $\Delta\Omega \to 0$, the rotordynamic coefficients, $K_{ee} - \Omega^2 M_{ee}$, $K_{e\alpha} - \Omega^2 M_{e\alpha}$, $K_{\alpha e} - \Omega^2 M_{\alpha e}$, $K_{\alpha\alpha} - \Omega^2 M_{\alpha\alpha}$, C_{ee}, $C_{e\alpha}$, $C_{\alpha e}$, $C_{\alpha\alpha}$ remain unchanged.

The identified coefficients are transformed from the (e, α) coordinate system to the (η, ξ) directions through the angle θ shown in Figure 2. Since the (η, ξ) are parallel to the corresponding fixed (x, y) and differ only in origin, no further rotation is required. The stiffness and damping coefficients in the coordinate system of (x, y) is therefore stated as:

$$\begin{bmatrix} K_{yy} - \Omega^2 M_{yy} & K_{yx} - \Omega^2 M_{yx} \\ K_{xy} - \Omega^2 M_{xy} & K_{xx} - \Omega^2 M_{xx} \end{bmatrix} = \begin{bmatrix} \sin\theta & \cos\theta \\ \cos\theta & -\sin\theta \end{bmatrix} \begin{bmatrix} K_{ee} - \Omega^2 M_{ee} & K_{e\alpha} - \Omega^2 M_{e\alpha} \\ K_{\alpha e} - \Omega^2 M_{\alpha e} & K_{\alpha\alpha} - \Omega^2 M_{\alpha\alpha} \end{bmatrix} \begin{bmatrix} \sin\theta & \cos\theta \\ \cos\theta & -\sin\theta \end{bmatrix} \tag{11}$$

$$\begin{bmatrix} C_{yy} & C_{yx} \\ C_{xy} & C_{xx} \end{bmatrix} = \begin{bmatrix} \sin\theta & \cos\theta \\ \cos\theta & -\sin\theta \end{bmatrix} \begin{bmatrix} C_{ee} & C_{e\alpha} \\ C_{\alpha e} & C_{\alpha\alpha} \end{bmatrix} \begin{bmatrix} \sin\theta & \cos\theta \\ \cos\theta & -\sin\theta \end{bmatrix} \tag{12}$$

The direct complex stiffness coefficient H_R, the average direct damping coefficient C_{avg}, the cross-coupled complex stiffness coefficient h_R and the effective damping coefficient C_{eff} are main factors to measure the rotordynamic performance of system [34]. Among them, H_R, h_R, C_{avg}, and C_{eff} are defined as:

$$\begin{cases} H_R = \left[\left(K_{xx} - \Omega^2 M_{xx} \right) + \left(K_{yy} - \Omega^2 M_{yy} \right) \right] / 2 \\ h_R = K_{xy} - \Omega^2 M_{xy} \\ C_{\mathrm{avg}} = \left(C_{xx} + C_{yy} \right) / 2 \\ C_{\mathrm{eff}} = C_{\mathrm{avg}} - h_R / \Omega \end{cases} \tag{13}$$

where C_{xx} and C_{yy} are the direct damping coefficients in the x and y directions, K_{xy} is the cross-coupled stiffness coefficient, K_{xx}, K_{yy} are the direct stiffness coefficient. M_{xx}, M_{yy}, M_{xy}, are the direct and cross-coupled inertial coefficients.

In summary, the identification procedure involves three main steps: (1) transient CFD simulations under small-amplitude circular whirling excitations are performed to extract the transient fluid forces; (2) the variation curve of the fluid force difference between $t = 0$ and $t = \mathrm{T}/4$ with respect to whirling frequency is constructed; and (3) by utilizing the tangent slope and intercept methods, the combined stiffness-inertia terms and damping terms are obtained, which are then transformed via coordinate transformations (Equations (11)–(13)) to yield the final stiffness and damping coefficients.

2.3. Computational Model

The present simulations were performed by solving the compressible RANS equations using a commercial CFD solver, ANSYS CFX (2026 R1). The numerical settings used in this study are summarized in Table 2. To accurately account for the real gas thermophysical properties of S-CO_2, an S-CO_2.rgp property file was generated from the NIST REFPROP database based on the Span–Wagner equation of state [35], and imported into the CFD solver. The compressibility factor is $Z = P/\rho RT$, where P is local pressure, ρ is density, T is absolute temperature, and R is the gas constant. Selected thermophysical properties are listed in Table 3. As shown in the table, under isothermal conditions (318.15 K), a 5.2% increase in pressure leads to a 12.3% increase in density. Under isobaric conditions (8.1 MPa), a 25.2% increase in temperature leads to a 49.0% decrease in density. These quantitative comparisons confirm that the strong nonlinear property variations necessitate real gas modeling to ensure thermodynamic validity.

Table 2. Calculation conditions.

Parameter	Value
Fluid	S-CO_2, Air (ideal gas)
Wall properties	Adiabatic, smooth surface
Temperature T/K	318.15, 358.15, 398.15
Time step/s	$1/(1000 \times \Omega_i)$ $(i = 1, 2, 3, ..., n)$
Whirling frequency Ω_i/Hz	20, 40, ..., 240, 260
Supply pressure P_{in}/MPa	7.7, 7.9, 8.1
Discharge pressure P_{out}/MPa	7.5
Rotational speed ω/rpm	10,000, 15,000, 20,000
Whirling orbit	Circle orbit
Vibration amplitude	6%C_r, 10%C_r
Eccentricity ratio	0

Table 3. Physical properties of S-CO_2.

Temperature (K)	Pressure (MPa)	Density (kg/m^3)	Enthalpy (kJ/kg)	Entropy [kJ/(kg·K)]	Viscosity (μPa·s)	Compressibility Factor
318.15	7.7	221.16	429.53	1.7461	20.311	0.579
318.15	7.9	234.11	424.82	1.7286	20.788	0.561
318.15	8.1	248.34	419.76	1.7100	21.341	0.543
358.15	8.1	157.43	498.16	1.9439	20.201	0.760
398.15	8.1	126.74	551.25	2.0847	21.279	0.850

The standard k-ε model was adopted for turbulence closure, with an inlet turbulence intensity of 5% [36]. The rotor and stator walls were treated as adiabatic, smooth and no-slip boundaries. Total pressure and total temperature were prescribed at the inlet, while the average static pressure was specified at the outlet. The rotor whirling orbit was imposed using CFX expression language (CEL). A structured mesh was employed in the computational domain. Local mesh refinement was applied near the seal blades tips, where steep velocity and pressure gradients are expected. The scalable wall function was used to bridge the near-wall region and the turbulent core flow, with the near-wall mesh resolution satisfying $30 < y+ < 80$ throughout the domain [37,38]. A mesh independence test was conducted, and the final mesh contained approximately 1.57×10^6 elements for the 4-blade seal. The grid distribution of the 10-blade seal is shown in Figure 4.

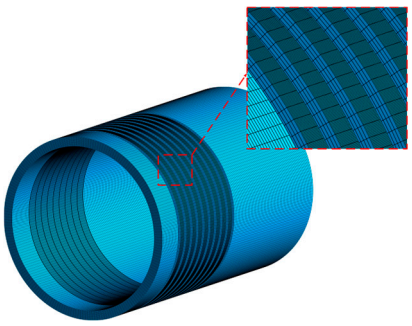


Figure 4. Grid distribution.

To verify the calculation accuracy and reliability of the present numerical method, a numerical simulation is carried out based on the experimental labyrinth seal model working with S-CO_2 [39]. As shown in Figure 5, the inlet pressure is set at 10 MPa, and the temperature is 318.15 K. The leakage flowrates of 13 different pressure ratios (0.3–0.9)

were calculated and compared with the experimental results. As shown in Figure 6, the calculation error is less than 8%. The current numerical method can accurately predict the leakage performance of the S-CO_2 labyrinth seal.

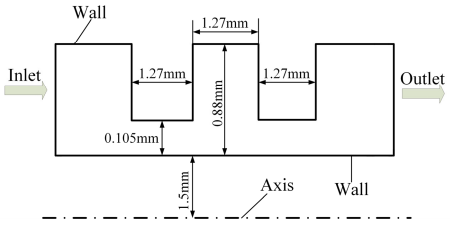


Figure 5. The experimental see-through labyrinth seal [39].

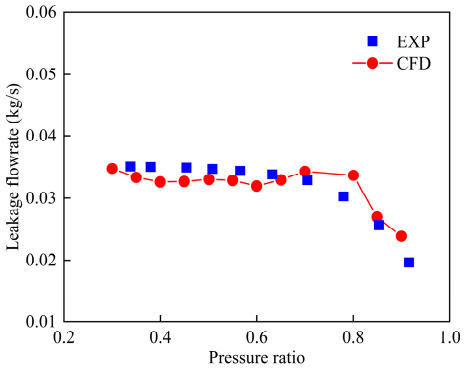


Figure 6. Experiment and CFD results of the leakage flowrate vs. pressure ratio for S-CO_2.

To assess the accuracy of the CFD method in predicting seal rotordynamic characteristics, the rotordynamic coefficients of the seal investigated in Ref. [40] were identified. Figures 7–10 compare the predicted direct stiffness, cross-coupled stiffness, direct damping, and effective damping coefficients, respectively, with the experimental data reported in Ref. [40]. The predicted coefficients agree well with the experimental data in both trend and magnitude. Specifically, the direct stiffness matches the experimental trend well and shows high consistency at high frequencies. For the effective damping coefficient, a key parameter for seal stability, the relative error is less than 20% at the running frequency and half-frequency, where fluid-induced excitation typically occurs. This demonstrates the accuracy and reliability of the CFD method for identifying seal rotordynamic coefficients, and this method is therefore adopted for the subsequent rotordynamic analysis.

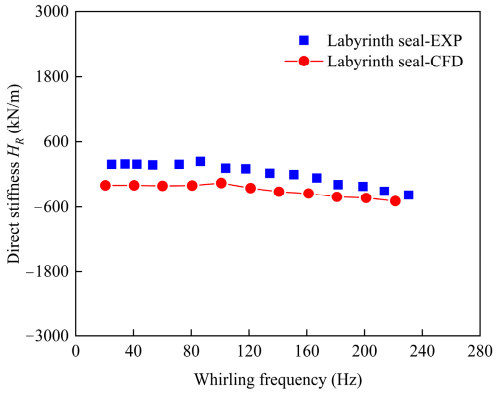


Figure 7. Direct complex stiffness coefficient vs. whirling frequency.

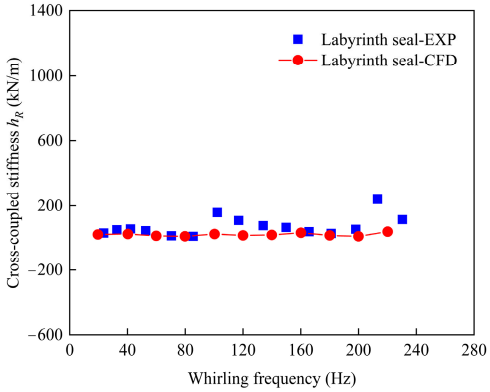


Figure 8. Cross-coupled complex stiffness coefficient vs. whirling frequency.

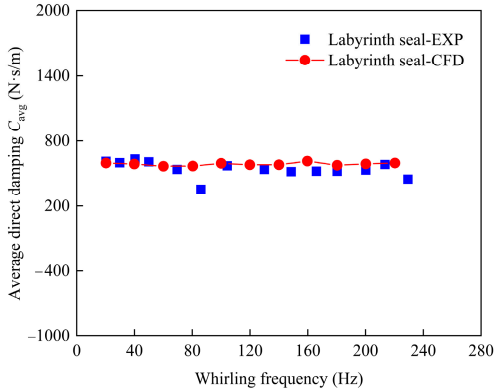


Figure 9. Average direct damping coefficient vs. whirling frequency.

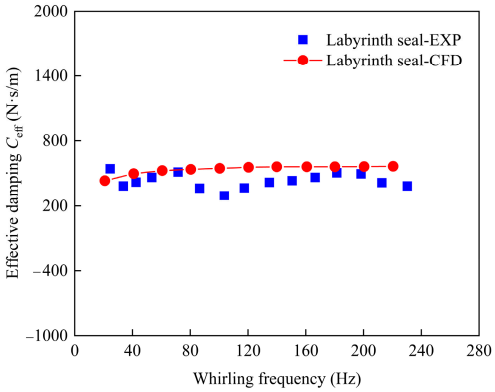


Figure 10. Effective damping coefficient vs. whirling frequency.

3. Results and Discussion

The rotordynamic behavior of the labyrinth seal is evaluated using the direct complex stiffness coefficient H_R, cross-coupled complex stiffness coefficient h_R, average direct damping coefficient C_{avg}, and effective damping coefficient C_{eff}. Among these parameters, C_{eff} is an important indicator of the stabilizing contribution of seal fluid forces because it combines the contribution of direct damping and cross-coupled stiffness. According to the definition $C_{\mathrm{eff}} = C_{\mathrm{avg}} - h_R/\Omega$, the variation in C_{eff} depends not only on the magnitude of C_{avg}, but also on the sign and magnitude of h_R and the whirling frequency. Therefore, the strong frequency dependence of C_{eff} at low whirling frequencies is mainly caused by the term h_R/Ω. As the whirling frequency increases, the contribution of h_R/Ω becomes weaker, and C_{eff} gradually approaches the level controlled by C_{avg}. For the circular whirling

considered in this study, a positive C_{eff} indicates that the combined effect of direct damping and cross-coupled dynamic stiffness opposes rotor whirling. At the same whirling direction and frequency, a larger positive C_{eff} therefore indicates a stronger equivalent damping effect, contributing favorably to rotordynamic stability. Understanding its variation is important for seal design aimed at enhancing stability. These relationships provide the physical basis for understanding the following parametric results.

3.1. Working Conditions Analysis on the Dynamic Force Coefficients for S-CO_2 Seals

3.1.1. Inlet Pressures P_{in}

For S-CO_2 working dominated by strong real gas effects, variations in inlet pressure significantly affect density, pressure gradient, and momentum of leakage flow, thereby altering the fluid forces acting on the rotor surface within the seal and ultimately affecting the seal rotordynamic characteristics. Figures 11–14 present the identified rotordynamic coefficients of the seal at three inlet pressures of 7.7 MPa, 7.9 MPa, and 8.1 MPa.

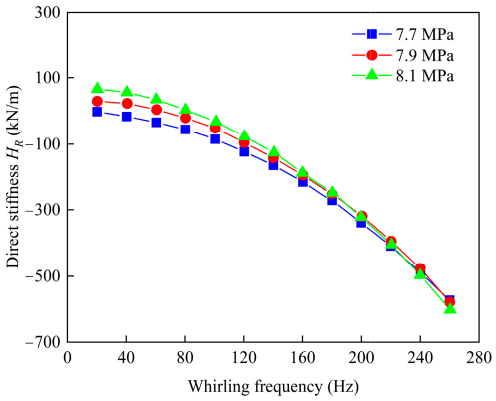


Figure 11. Direct complex stiffness coefficient vs. whirling frequency under different P_{in}.

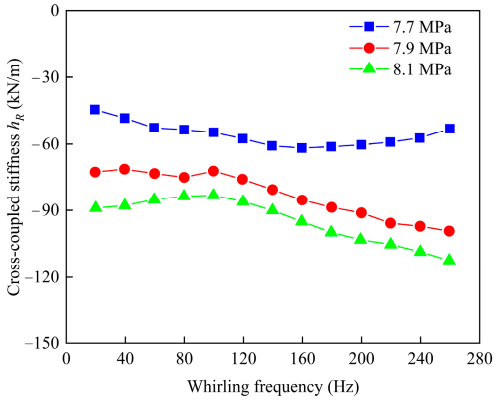


Figure 12. Cross-coupled complex stiffness coefficient vs. whirling frequency under different P_{in}.

Figure 11 shows that the direct complex stiffness coefficient H_R is highly dependent on whirling frequency. In the low-frequency range, inlet pressure has a significant effect on H_R. For example, at approximately 20 Hz, H_R changes from a slightly negative value at P_{in} = 7.7 MPa to about 60–70 kN/m at P_{in} = 8.1 MPa. However, with increasing whirling frequency, all curves decrease rapidly and become negative. At 260 Hz, H_R reaches approximately −570 to −600 kN/m for the three inlet pressures. This indicates that the inertial component included in the complex stiffness becomes dominant at high whirling frequencies, while the pressure-related stiffness contribution is more significant in the low-frequency range. Figure 12 shows that h_R remains negative over the whole frequency range.

The magnitude of h_R increases with inlet pressure. At 20 Hz, h_R is approximately −45 kN/m at 7.7 MPa and decreases to about −90 kN/m at 8.1 MPa. At 260 Hz, the corresponding values are approximately −53 kN/m and −113 kN/m. This means that increasing inlet pressure strengthens the circumferential pressure perturbation and the fluid-induced cross-coupled force. Physically, a higher inlet pressure increases the density and the pressure gradient across each blade, leading to stronger jet acceleration, cavity recirculation, and pressure redistribution around the rotor.

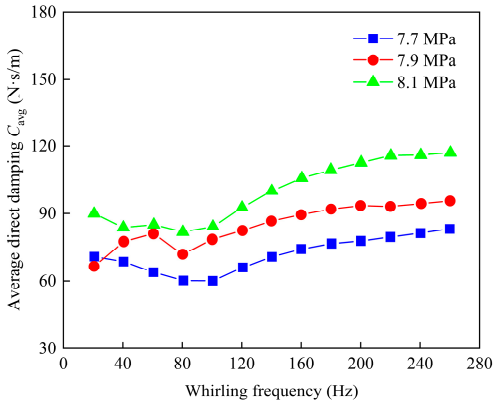


Figure 13. Average direct damping coefficient vs. whirling frequency under different P_{in}.

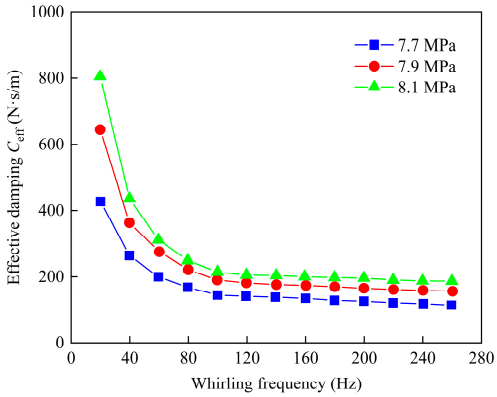


Figure 14. Effective damping coefficient vs. whirling frequency under different P_{in}.

The average direct damping coefficient C_{avg} also increases with inlet pressure, as shown in Figure 13. At high whirling frequencies, C_{avg} increases from about 84 N·s/m at 7.7 MPa to nearly 116~118 N·s/m at 8.1 MPa. This increase is associated with stronger momentum exchange and higher energy dissipation in the seal cavities. Since supercritical CO_2 has a relatively high density, the pressure fluctuation induced by rotor whirling can produce a stronger damping force under higher-pressure conditions. Figure 14 further confirms that the effective damping coefficient C_{eff} increases with inlet pressure. At 20 Hz, C_{eff} rises from approximately 430 N·s/m at 7.7 MPa to about 800 N·s/m at 8.1 MPa. At 260 Hz, the difference becomes smaller, but still increases from about 120 N·s/m to nearly 190 N·s/m. The sharp decrease in C_{eff} with frequency is mainly caused by the reduction in the h_R/Ω contribution.

Therefore, the stabilizing effect of inlet pressure is most evident in the low-frequency whirling region. As the whirling frequency increases, the curves for different pressures gradually converge. This frequency-dependent feature is attributed to the real gas effect, which makes density and pressure perturbation highly sensitive to inlet pressure. From the viewpoint of the seal's rotordynamic stability, increasing inlet pressure enhances the effective

damping capacity of the S-CO_2 labyrinth seal, although it also increases the magnitude of the cross-coupled stiffness.

3.1.2. Inlet Temperature *T*

Inlet temperature affects the unsteady pressure response and fluid dissipation characteristics within the seal by altering the density, compressibility, and thermophysical properties of S-CO_2, thereby changing the seal rotordynamic characteristics. Figures 15–18 present the identified rotordynamic coefficients of the seal at three inlet temperatures: 318.15 K, 358.15 K, and 398.15 K. Figures 15 and 16 show that inlet temperature has a strong influence on both H_R and h_R. As the inlet temperature increases from 318.15 K to 398.15 K, the magnitude of H_R decreases significantly. At 260 Hz, H_R is about −600 kN/m at 318.15 K, whereas it is only about −250 kN/m at 398.15 K. A similar trend is observed for h_R. At 260 Hz, h_R changes from approximately −113 kN/m at 318.15 K to about −73 kN/m at 398.15 K. This indicates that lower inlet temperature intensifies the fluid-induced dynamic force. The mechanism is closely related to the real gas properties of supercritical CO_2. When the inlet temperature decreases, especially near the critical region, the density of CO_2 increases and the thermophysical properties become more sensitive to pressure and temperature variations. Under the same pressure boundary condition, a lower temperature produces a denser working fluid in the seal clearance and cavities. As a result, rotor whirling induces larger pressure perturbations and stronger unsteady fluid forces. In contrast, increasing temperature weakens the density-related pressure response, resulting in smaller stiffness and cross-coupled force coefficients.

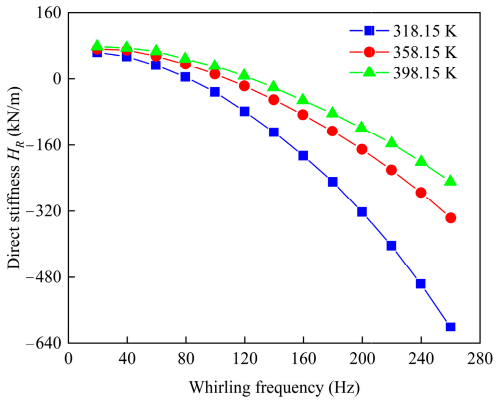


Figure 15. Direct complex stiffness coefficient vs. whirling frequency under different *T*.

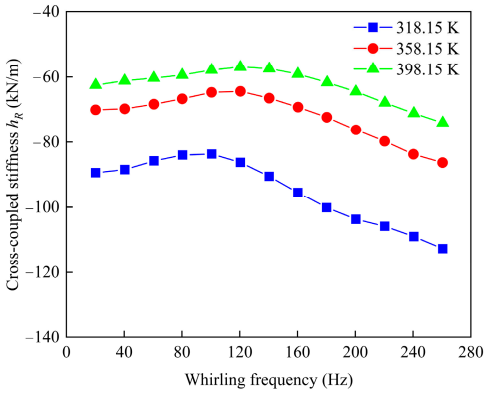


Figure 16. Cross-coupled complex stiffness coefficient vs. whirling frequency under different *T*.

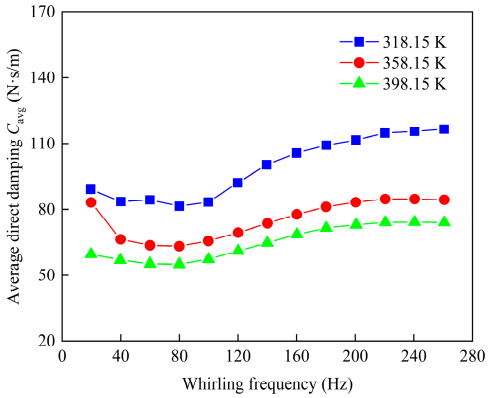


Figure 17. Average direct damping coefficient vs. whirling frequency under different *T*.

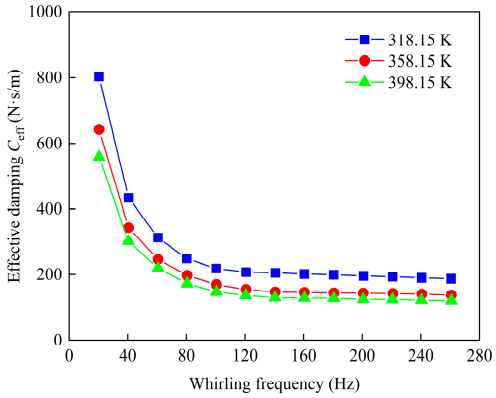


Figure 18. Effective damping coefficient vs. whirling frequency under different *T*.

To further examine the damping characteristics, Figures 17 and 18 show that both C_{avg} and C_{eff} decrease with increasing inlet temperature. At 260 Hz, C_{avg} decreases from about 118 N·s/m at 318.15 K to about 74 N·s/m at 398.15 K. The effective damping coefficient shows the same trend. At 20 Hz, C_{eff} decreases from nearly 800 N·s/m at 318.15 K to about 560 N·s/m at 398.15 K. At 260 Hz, it decreases from about 185 N·s/m to approximately 125 N·s/m. Therefore, a lower inlet temperature improves the damping capacity and stability of the seal.

This result suggests that the rotordynamic performance of S-CO_2 seals is highly sensitive to the thermodynamic state of the working fluid. Compared with ideal-gas seals, the rotordynamic coefficients of S-CO_2 seals are not determined only by pressure ratio and geometry, but also by the real gas-induced variation in density and compressibility. Therefore, accurate real gas property modeling is necessary when evaluating S-CO_2 seal stability.

3.1.3. Rotational Speeds ω

Rotational speed is a key parameter influencing the circumferential flow within the seal. By altering the swirl intensity and the non-uniform pressure distribution in the seal cavities, it modulates the competition between the cross-coupled fluid force and the direct damping. Figures 19–22 present the variations in rotordynamic coefficients with whirling frequency for three rotational speeds of 10,000, 15,000, and 20,000 rpm. Figures 19 and 20 show the influence of rotational speed on H_R and h_R. As the rotor speed increases from 10,000 rpm to 20,000 rpm, the magnitude of both coefficients increases. For example, at 260 Hz, H_R decreases from approximately −570 kN/m to about −620 kN/m. The change in h_R is more obvious. At 260 Hz, h_R decreases from about −70 kN/m at 10,000 rpm to nearly −160 kN/m at 20,000 rpm. The variation amplitude is considerably larger than that of the

former. This comparison indicates that rotational speed primarily governs the cross-coupled complex stiffness, while its influence on the direct complex stiffness is relatively limited.

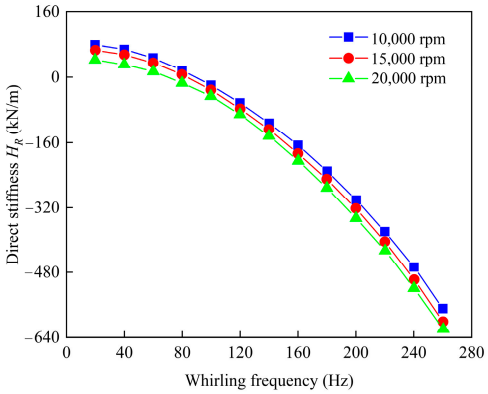


Figure 19. Direct complex stiffness coefficient vs. whirling frequency under different ω.

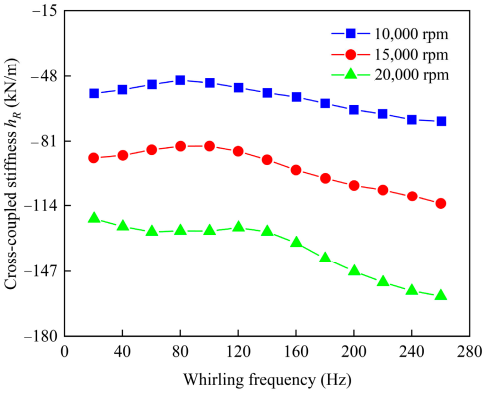


Figure 20. Cross-coupled complex stiffness coefficient vs. whirling frequency under different ω.

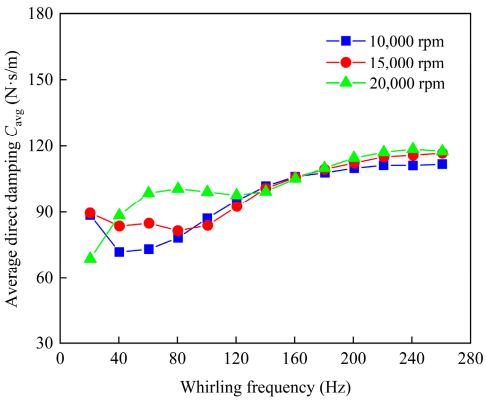


Figure 21. Average direct damping coefficient vs. whirling frequency under different ω.

To further inspect the damping characteristics, Figure 21 shows that C_{avg} is only slightly affected by rotational speed, especially at high whirling frequencies. In contrast, Figure 22 shows that C_{eff} increases significantly with rotational speed. At 20 Hz, C_{eff} increases from about 540 N·s/m at 10,000 rpm to more than 1000 N·s/m at 20,000 rpm. At 260 Hz, it increases from about 165 N·s/m to about 220 N·s/m. The difference between C_{avg} and C_{eff} indicates that the increase in effective damping is mainly caused by the variation in the h_R/Ω term, rather than by direct damping alone.

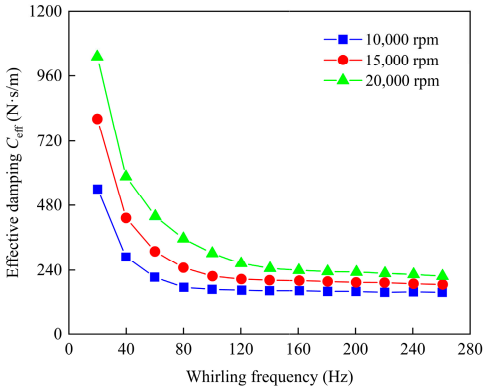


Figure 22. Effective damping coefficient vs. whirling frequency under different ω.

Therefore, under the present sign convention, the negative h_R contributes positively to C_{eff}. Increasing rotational speed strengthens the magnitude of h_R, and this contribution is especially pronounced at low whirling frequencies. However, it should also be noted that a stronger cross-coupled force may not always be beneficial in other sign conventions or operating conditions. Thus, the stability assessment should be based on the combined effective damping coefficient rather than on a single dynamic coefficient.

3.2. Geometries Analysis on the Dynamic Force Coefficients for S-CO_2 Seals

3.2.1. Blade Quantities

The number of blades is an important geometric parameter that determines the complexity of the leakage path. By changing the number of throttling stages and cavities, it affects the fluid pressure distribution, energy dissipation process, and unsteady fluid force response, thereby modulating the frequency-dependent response of the rotordynamic coefficients. Figures 23–26 present the identified rotordynamic coefficients of the seal for different numbers of blades. Figures 23 and 24 show that increasing the number of blades significantly changes the stiffness-related coefficients. At 260 Hz, H_R is only about −60 kN/m for the 4-blade seal, whereas it decreases to approximately −520 kN/m for the 10-blade seal. The magnitude of h_R also increases with blade number. At 260 Hz, h_R changes from about −20 kN/m for 4 blades to nearly −78 kN/m for 10 blades. This indicates that adding more blades strengthens the pressure perturbation and the dynamic force response of the seal.

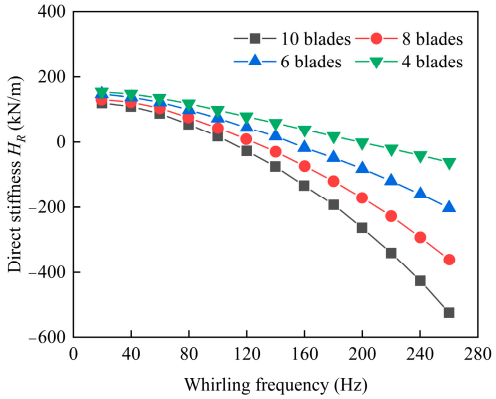


Figure 23. Direct complex stiffness coefficient vs. whirling frequency under different quantities.

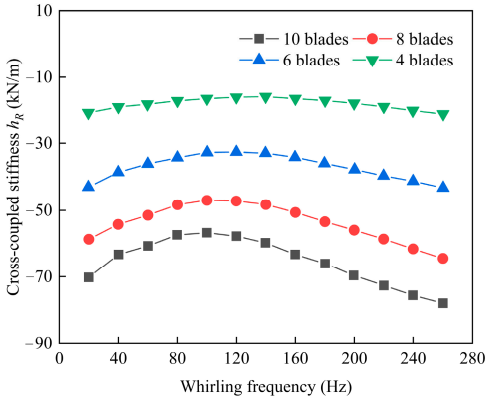


Figure 24. Cross-coupled complex stiffness coefficient vs. whirling frequency under different quantities.

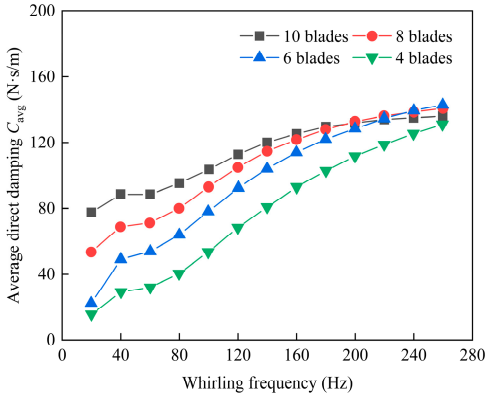


Figure 25. Average direct damping coefficient vs. whirling frequency under different quantities.

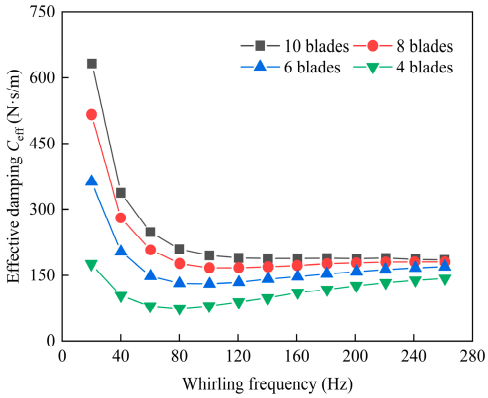


Figure 26. Effective damping coefficient vs. whirling frequency under different quantities.

As shown in Figure 25, C_{avg} increases with blade number, especially at low and medium whirling frequencies. At 20 Hz, C_{avg} increases from about 15 N·s/m for 4 blades to about 78 N·s/m for 10 blades. At high frequencies, the differences become smaller because the damping coefficient gradually approaches a saturated level. Figure 26 shows that C_{eff} also increases with blade number. At 20 Hz, C_{eff} increases from about 175 N·s/m for 4 blades to more than 600 N·s/m for 10 blades. At 260 Hz, the difference is reduced, but the 10-blade seal still shows the highest effective damping. The leakage flow experiences repeated acceleration through the blade clearance and expansion in the cavity. This repeated throttling–expansion process enhances jet breakup, vortex formation, and turbulent mixing. Consequently, more kinetic energy is dissipated in the cavities, and the pressure drop is

distributed over more sealing stages. This improves the damping-related performance of the seal.

These results indicate that increasing blade quantity is beneficial for improving seal stability, especially in the low-frequency whirling region. However, the improvement is not linear over the entire frequency range. When the blade number becomes large, additional blades mainly increase the flow resistance and cavity dissipation, while the marginal increase in C_{eff} becomes smaller at high frequencies. Therefore, blade number should be optimized by considering both leakage reduction and damping enhancement.

3.2.2. Sealing Clearances

The sealing clearance is an important geometric parameter that affects the leakage flow state and fluid dynamic response. Its variation not only changes the throttling capacity of the seal but also influences the pressure gradient near the blade tip, cavity momentum exchange, and unsteady fluid force distribution, thereby altering the stability control mechanism over different frequency ranges. Figures 27–30 present the identified rotordynamic coefficients of the seal for different sealing clearances. Figures 27 and 28 show that the magnitudes of H_R and h_R decrease as the sealing clearance increases. At 260 Hz, H_R changes from about −550 kN/m for the 0.16 mm clearance to about −420 kN/m for the 0.32 mm clearance. Similarly, h_R changes from approximately −88 kN/m to about −53 kN/m. This means that a smaller clearance produces stronger pressure and cross-coupled force. The reason is that reducing the clearance increases the flow restriction and strengthens the local pressure gradient near the blade tip. The rotor whirling motion then causes larger circumferential pressure differences, leading to larger stiffness.

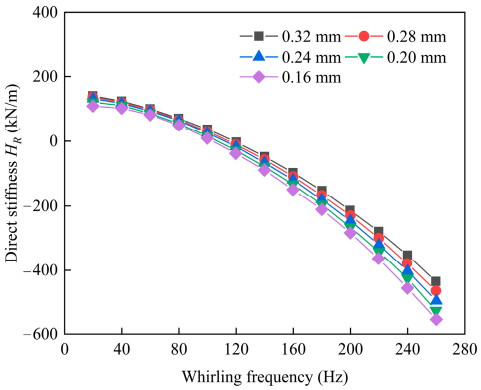


Figure 27. Direct complex stiffness coefficient vs. whirling frequency under different sealing clearances.

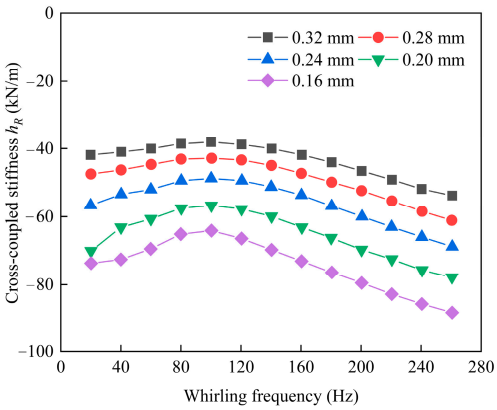


Figure 28. Cross-coupled complex stiffness coefficient vs. whirling frequency under different sealing clearances.

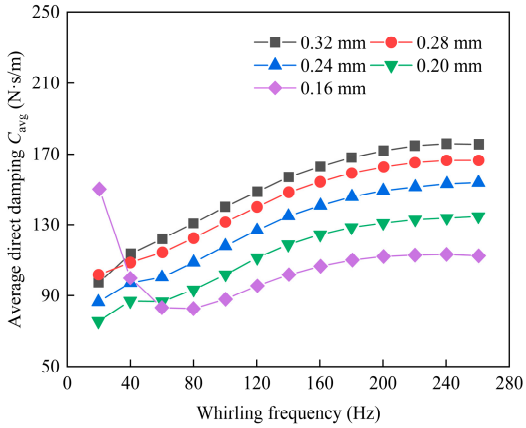


Figure 29. Average direct damping coefficient vs. whirling frequency under different sealing clearances.

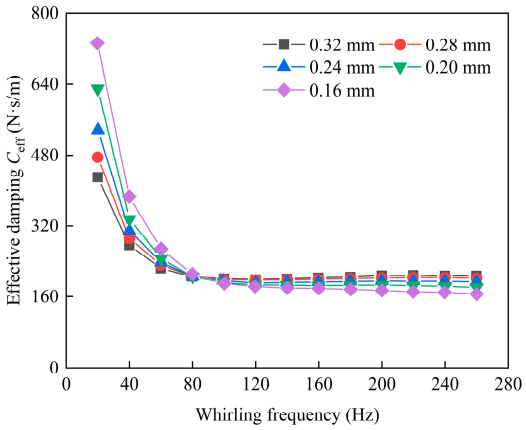


Figure 30. Effective damping coefficient vs. whirling frequency under different sealing clearances.

However, the damping coefficients show a more complicated trend. Figure 29 indicates that increasing clearance can increase C_{avg}. At high whirling frequencies, C_{avg} increases from about 114 N·s/m for 0.16 mm to about 176 N·s/m for 0.32 mm. Figure 30 shows that the effect of clearance on C_{eff} depends strongly on whirling frequency. At low whirling frequencies, smaller clearance gives a much higher C_{eff}. At 20 Hz, C_{eff} is about 730 N·s/m for 0.16 mm, while it is about 430 N·s/m for 0.32 mm. This is because the h_R/Ω term dominates C_{eff} at low frequencies, and the smaller clearance produces a larger magnitude of h_R. As the whirling frequency increases, the influence of h_R/Ω becomes weaker, and C_{eff} is increasingly controlled by C_{avg}. Therefore, at high frequencies above about 80 Hz, larger clearance leads to slightly higher C_{eff}. At 260 Hz, C_{eff} is approximately 170 N·s/m for 0.16 mm and about 210 N·s/m for 0.32 mm.

These results show that clearance optimization should consider the operating whirling-frequency range. For low-frequency rotor whirling, a smaller clearance is favorable for improving effective damping. For high-frequency whirl, a slightly larger clearance may provide higher direct damping. Therefore, the clearance effect cannot be judged only by leakage performance; it should be evaluated together with rotordynamic stability of the seal.

3.3. Different Working Fluids Analysis on the Dynamic Force Coefficients

Since the thermophysical properties of the working fluid directly govern fluid inertia, compressibility, and energy dissipation capacity, variations in the working fluid fundamentally alter the fluid dynamic response characteristics of the seal. This section compares S-CO_2

and air as two distinct engineering working fluids. Figures 31–34 present the identified rotordynamic coefficients of the seal for air and S-CO_2.

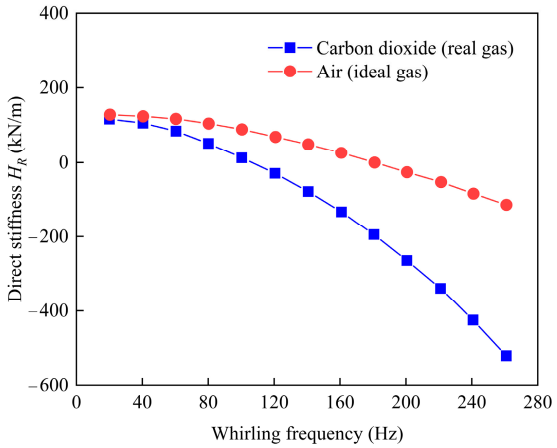


Figure 31. Direct complex stiffness coefficient vs. whirling frequency under different fluids.

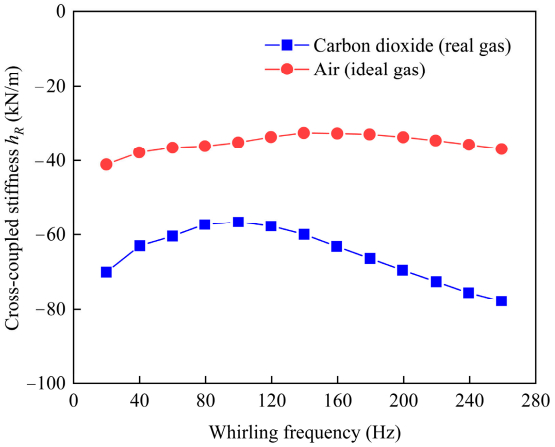


Figure 32. Cross-coupled complex stiffness coefficient vs. whirling frequency under different fluids.

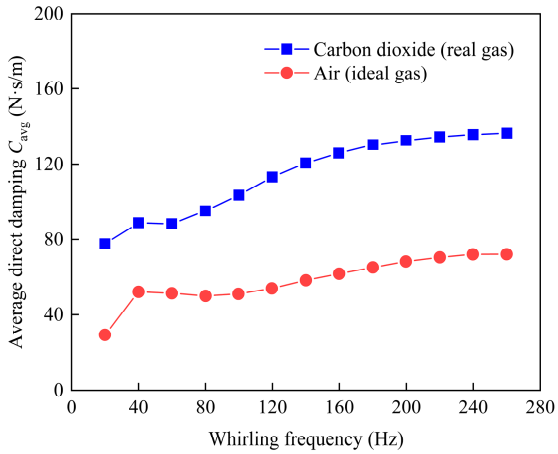


Figure 33. Average direct damping coefficient vs. whirling frequency under different fluids.

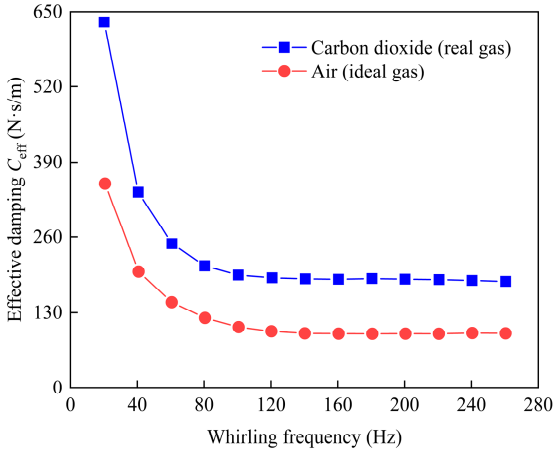


Figure 34. Effective damping coefficient vs. whirling frequency under different fluids.

Figures 31 and 32 compare the dynamic stiffness coefficients of the labyrinth seal with S-CO_2 and air. The H_R of the S-CO_2 seal shows a much stronger frequency dependence than that of the air seal. At 260 Hz, H_R reaches approximately −520 kN/m for S-CO_2, whereas it is only about −115 kN/m for air. The magnitude of h_R is also higher for S-CO_2. At 260 Hz, h_R is about −78 kN/m for S-CO_2 and about −36 kN/m for air. This difference is mainly attributed to the much higher density of S-CO_2 than that of air, which allows the same rotor whirl to induce larger pressure perturbations and stronger fluid inertia effects within the seal clearance and cavities. In addition, the real gas compressibility of S-CO_2 causes stronger coupling between pressure, density, and temperature, making the dynamic response of the seal more sensitive to operating conditions. Figures 33 and 34 show that the damping coefficients of the S-CO_2 seal are also higher than those of the air seal. At 260 Hz, C_{avg} is about 136 N·s/m for S-CO_2 and about 72 N·s/m for air. The effective damping coefficient of the S-CO_2 seal is about 167~202% of that of the air seal over the investigated frequency range. At 20 Hz, C_{eff} is approximately 630 N·s/m for S-CO_2 and about 350 N·s/m for air. At 260 Hz, C_{eff} remains about 185 N·s/m for S-CO_2, while it is about 95 N·s/m for air.

These results demonstrate that the S-CO_2 labyrinth seal has stronger rotordynamic force coefficients than the air seal. More importantly, the increase in direct and effective damping is larger than the destabilizing contribution associated with cross-coupled stiffness under the present operating conditions. Therefore, the S-CO_2 seal exhibits better stability for the seal segment than the air seal. However, the stronger stiffness and cross-coupled force also imply that the real gas effect should not be neglected in rotordynamic design. Using air-based or air (ideal-gas) assumptions would underestimate both the damping capacity and the fluid-induced force level of S-CO_2 labyrinth seals. This combined effect on the seal's rotordynamic performance, arising from the real gas equation of state and inherent molecular property differences, provides comprehensive engineering guidance for actual S-CO_2 turbomachinery design.

4. Conclusions

This study presents a comprehensive investigation of the rotordynamic performance of the labyrinth seal working with supercritical carbon dioxide (S-CO_2). A computational fluid dynamics method is employed to establish a full three-dimensional numerical model for the labyrinth seal. An identification method based on the infinitesimal theory is applied to obtain the dynamic force coefficients. The CFD model predicts the dynamic force coefficients for the seals operating under various inlet pressures, temperatures, rotational speeds, blade quantities, and sealing clearances conditions. Several conclusions are summarized as follows.

(1) The direct complex stiffness coefficient of the labyrinth seal working with S-CO_2 has a strong frequency dependency, while the cross-coupled complex stiffness coefficient and average direct damping coefficient have relatively small frequency dependence.
(2) The effective damping coefficient of the labyrinth seal working with S-CO_2 increases with the increasing inlet pressure, rotational speed and blade quantities, and decreases as the inlet temperature increases. The effective damping coefficient has a strong frequency dependence at low whirling frequencies (less than ~80 Hz) and increases slightly with the decreasing sealing clearance. At high whirling frequencies (above ~80 Hz), the effective damping coefficient increases with the increasing sealing clearance. This frequency-dependent behavior is closely related to the real gas properties of S-CO_2.
(3) The effective damping coefficient of the labyrinth seal working with S-CO_2 is about 167~202% of that with air. The frequency dependence of H_R for S-CO_2 is much stronger than that for air, especially in the high-frequency region. This improvement is mainly attributed to the high density, real gas compressibility of S-CO_2, which enhance pressure perturbation, momentum exchange, and cavity dissipation during rotor whirling. Therefore, the real gas effect should be included in the rotordynamic design and stability evaluation of S-CO_2 turbomachinery seals.

Overall, this study investigates the frequency-dependent rotordynamic characteristics of S-CO_2 labyrinth seals over a broad range and clarifies the differences compared to air (ideal gas) models under identical conditions. The coefficients identified herein provide a reliable foundation for future work to incorporate bearing characteristics and rotor dynamics into evaluations of the complete S-CO_2 rotor–bearing–seal system.

Author Contributions: Conceptualization, W.Z. and Q.G.; methodology, C.L. and J.Y.; software, Q.Z. and W.W.; investigation, M.Y. and J.Y.; data curation, Q.Z. and W.W.; writing—original draft preparation, Q.Z.; writing—review and editing, W.Z. and Q.G.; visualization, W.M.; supervision, W.Z.; funding acquisition, W.Z. and Q.G. All authors have read and agreed to the published version of the manuscript.

Funding: The authors are grateful for grants from the National Natural Science Foundation of China (52375193), the Natural Science Foundation of Shanghai (25ZR1402381) and the Shanghai Science and Technology Plan Project (24TS1416000).

Data Availability Statement: The data are available from the corresponding author upon reasonable request.

Conflicts of Interest: The authors declare no conflicts of interest.

Abbreviations

The following abbreviations are used in this manuscript:

S-CO_2	Supercritical carbon dioxide
CFD	Computational fluid dynamics
RANS	Reynolds-averaged Navier–Stokes
NIST	National Institute of Standards and Technology
REFPROP	Reference Fluid Thermodynamic and Transport Properties
CEL	CFX expression language

References

1. Manesh, M.H.K.; Ghorbani, S.; Blanco-Marigorta, A.M. Optimal design and analysis of a combined freshwater-power generation system based on integrated solid oxide fuel cell-gas turbine-organic Rankine cycle-multi effect distillation system. *Appl. Therm. Eng.* **2022**, *211*, 118438. [CrossRef]

2. Chen, J.; Cheng, K.; Li, X.; Huai, X.; Dong, H. Thermodynamic evaluation and optimization of supercritical CO_2 Brayton cycle considering recuperator types and designs. *J. Clean. Prod.* **2023**, *414*, 137615. [CrossRef]
3. Lin, M.; Guo, C.; Li, Z.; Zhao, D.; Zhang, H.; Wang, B.; Xu, X. Effect of internal losses on the thermodynamic performance of a supercritical carbon dioxide Brayton cycle system. *Energy* **2025**, *341*, 139450. [CrossRef]
4. Tello, C.; Muñoz, A.; Sánchez, D.; Kipouros, T.; Savill, M. Impact of fluid substitution on the performance of an axial compressor blade cascade working with supercritical carbon dioxide. *J. Eng. Gas. Turbines Power* **2020**, *142*, 011019. [CrossRef]
5. Zhang, P.; Wang, Z.; Zhang, Y.; Wang, F. Study on the impact of a novel honeycomb gas cooler on the performance and discharge pressure control of a transcritical CO_2 heat pump system. *J. Mech. Sci. Technol.* **2025**, *39*, 1487–1501. [CrossRef]
6. Du, Y.; Yang, C.; Zhao, B.; Wang, H.; Zhang, H.; He, X.; Hu, C.; Li, Y. Investigation of off-design performance of supercritical carbon dioxide recompression cycle using a deep learning-based turbine with variable inlet guide vanes. *Energy Convers. Manag.* **2023**, *286*, 117068. [CrossRef]
7. Li, J.; Shi, D.; Zhu, G.; Xie, Y. A multi-factor comprehensive optimization of a supercritical carbon dioxide radial inflow turbine with low specific speed. *J. Mech. Sci. Technol.* **2022**, *36*, 5059–5074. [CrossRef]
8. Gu, Q.; Wu, W.; Zhang, W.; Zhang, Q.; Zhang, X.; Li, C.; Yue, M.; Miao, W.; Yang, J. A self-twisting flow seal for leakage reduction via global leakage path reconfiguration. *Tribol. Int.* **2026**, *223*, 112235. [CrossRef]
9. Kim, B.; Kim, H.S.; Suh, J.; Kwak, H.-D. Prediction of lateral and angular eccentricity effects on plain annular seal performance using transient 3D CFD. *J. Mech. Sci. Technol.* **2025**, *39*, 3039–3048. [CrossRef]
10. Ma, C.; Bai, S. A heat transfer model for thermal distortions in high speed spiral groove gas lubricated face seals. *Tribol. Int.* **2025**, *203*, 110408. [CrossRef]
11. Zhang, M.; Yang, J.; Zhang, W.; Gu, Q. Turbomachines seal flow resistance enhancement and leakage reduction based on flow control method with bow-shaped auxiliary teeth. *Energy* **2024**, *300*, 131631. [CrossRef]
12. Zaniewski, D.; Klimaszewski, P.; Klonowicz, P.; Lampart, P.; Witanowski, Ł.; Jędrzejewski, Ł.; Suchocki, T.; Antczak, Ł. Performance of the honeycomb type sealings in organic vapour microturbines. *Energy* **2021**, *226*, 120242. [CrossRef]
13. Dostal, V. A Supercritical Carbon Dioxide Cycle for Next Generation Nuclear Reactors. Ph.D. Thesis, Massachusetts Institute of Technology, Cambridge, MA, USA, 2004.
14. Lanjewar, S.; Kumar, P.; Gopi, P.C. Effect of fluid barrier in see-through labyrinth seal for supercritical CO_2 turbomachinery. *J. Eng. Gas. Turbines Power* **2026**, *148*, 011023. [CrossRef]
15. Zhang, E.; Xu, H.; Li, J.; Bai, B. Turbulence dissipation of leakage flow in supercritical CO_2 labyrinth seals. *Prog. Nucl. Energy* **2022**, *151*, 104336. [CrossRef]
16. Yin, L.; Zhang, W.; Jiang, G.; Pan, B.; Li, C. Research on the dynamic stability of high and low tooth comb seals in supercritical carbon dioxide. *Tribology* **2021**, *41*, 115–124. (In Chinese) [CrossRef]
17. Xu, H.; Chen, W.; Deng, Q.; Sun, X.; Mao, W. Dynamic characteristics of carbon dioxide spiral groove dry gas seal influenced by real gas effect. *Proc. Inst. Mech. Eng. Part J. J. Eng. Tribol.* **2026**, *240*, 952–963. [CrossRef]
18. Odabaee, M.; Sauret, E.; Hooman, K. CFD simulation of a supercritical carbon dioxide radial-inflow turbine, comparing the results of using real gas equation of estate and real gas property file. *Appl. Mech. Mater.* **2016**, *846*, 85–90. [CrossRef]
19. Zeng, C.; Zhou, Y.; Huang, Y.; Tian, G.; Huang, J.; Zang, J. Influence of physical-property variations on leakage for supercritical CO_2 seal. *Int. J. Greenh. Gas. Control* **2023**, *129*, 103989. [CrossRef]
20. Xiong, C.; Xu, B.; Chen, Z. Flow and thermo-hydrodynamic characteristics in supercritical CO_2 lubrication. *Appl. Therm. Eng.* **2024**, *241*, 122399. [CrossRef]
21. Si, H.; Yu, Z.; Cao, L.; Chen, D. Seal dynamics of supercritical carbon dioxide turbine with the uncertain rotor nonlinear motion. *Aerosp. Sci. Technol.* **2024**, *154*, 109493. [CrossRef]
22. Lu, B.; Zhang, S.; Huo, E.; Yu, Y.; Huang, R.; Yin, J.; Wang, S. Shaft seal leakage-affected off-design performance, safety margins and control strategy evaluation of recompression supercritical CO_2 direct cooled reactor Brayton cycle. *Energy* **2026**, *356*, 141282. [CrossRef]
23. Bidkar, R.A.; Sevincer, E.; Wang, J.; Thatte, A.M.; Mann, A.; Peter, M.; Musgrove, G.; Allison, T.; Moore, J. Low-leakage shaft-end seals for utility-scale supercritical CO_2 turboexpanders. *J. Eng. Gas. Turbines Power* **2017**, *139*, 022503. [CrossRef]
24. Yuan, T.; Li, Z.; Li, J.; Yuan, Q. Static and rotordynamic characteristics for supercritical carbon dioxide spiral groove dry gas seal with the tilted seal ring. *J. Eng. Gas. Turbines Power* **2023**, *145*, 011011. [CrossRef]
25. Zhang, E.; Li, Y.; Lai, Z.; Bai, B. Leakage flow-induced excitation behavior and rotor instability in the high-speed supercritical CO_2 scallop damper seals. *Phys. Fluids* **2024**, *36*, 036121. [CrossRef]
26. Zhang, E.; Watanabe, T.; Himeno, T.; Bai, B. Leakage reduction mechanism of supercritical CO_2 scallop damper seal: Vortex structure and turbulence dissipation. *Phys. Fluids* **2023**, *35*, 056108. [CrossRef]
27. Zhu, Y.; Jiang, Y.; Liang, S.; Guo, Y.; Guo, C.; Yue, P. Numerical study of super-critical carbon dioxide flow in stepped-staggered labyrinth seals. In Proceedings of the 6th International Supercritical CO_2 Power Cycles Symposium, Pittsburgh, PA, USA, 27–29 March 2018.

28. Li, Z.; Zhang, Z.; Li, J. Sensitivity analysis of the static and rotordynamic characteristics on geometric parameters for a supercritical carbon dioxide hole-pattern damper seal. *J. Eng. Gas. Turbines Power* **2025**, *147*, 011005. [CrossRef]
29. Xie, Y.; Wang, Y.; Zhang, D.; Shi, D. Research progress on supercritical carbon dioxide Brayton cycle system and turbomachinery. *Proc. CSEE* **2018**, *38*, 7276–7286+7454. (In Chinese) [CrossRef]
30. Si, H.; Wang, Y.; Cao, L.; Chen, D. Dynamic behavior of seal-rotor system in a supercritical carbon dioxide turbine during acceleration transition. *Acta Aeronaut. Astronaut. Sin.* **2024**, *45*, 228652. (In Chinese) [CrossRef]
31. Comsa, C.; Cizmas, P.G.A. An experimental and numerical investigation of the rotordynamic force coefficients of a gas labyrinth seal: Part 2—Numerical simulation. *Tribol. Trans.* **2026**, *69*, 562–572. [CrossRef]
32. Comsa, C.; Hyun, H.S.; Delgado, A.; Cizmas, P.G.A. An experimental and numerical investigation of the rotordynamic force coefficients of a gas labyrinth seal: Part 1—Experimental results. *Tribol. Trans.* **2026**, *69*, 549–561. [CrossRef]
33. Zhang, W.; Gu, Q.; Yang, J.; Li, C. Application of a novel rotordynamic identification method for annular seals with arbitrary elliptical orbits and eccentricities. *J. Eng. Gas. Turbines Power* **2019**, *141*, 091016. [CrossRef]
34. San Andrés, L.; Yang, J.; Lu, X. On the leakage, torque, and dynamic force coefficients of air in oil (wet) annular seal: A computational fluid dynamics analysis anchored to test data. *J. Eng. Gas. Turbines Power* **2019**, *141*, 021008. [CrossRef]
35. White, C.W.; Weiland, N.T. Evaluation of property methods for modeling direct-supercritical CO_2 power cycles. *J. Eng. Gas. Turbines Power* **2018**, *140*, 011701. [CrossRef]
36. Zhao, Y.; Wang, C. Shape optimization of labyrinth seals to improve sealing performance. *Aerospace* **2021**, *8*, 92. [CrossRef]
37. Grotjans, H.; Menter, F.R. Wall functions for general application CFD codes. In *Computational Fluid Dynamics '98*; Papailiou, K.D., Tsahalis, D., Periaux, J., Hirsch, C., Pandolfi, M., Eds.; John Wiley & Sons: Chichester, UK, 1998; pp. 1112–1117.
38. Kalitzin, G.; Medic, G.; Iaccarino, G.; Durbin, P. Near-wall behavior of RANS turbulence models and implications for wall functions. *J. Comput. Phys.* **2005**, *204*, 265–291. [CrossRef]
39. Yuan, H.; Pidaparti, S.; Wolf, M.; Edlebeck, J.; Anderson, M. Numerical modeling of supercritical carbon dioxide flow in see-through labyrinth seals. *Nucl. Eng. Des.* **2015**, *293*, 436–446. [CrossRef]
40. Ertas, B.H.; Delgado, A.; Vannini, G. Rotor dynamic force coefficients for three types of annular gas seals with inlet preswirl and high differential pressure ratio. *J. Eng. Gas. Turbines Power* **2012**, *134*, 042503–042514. [CrossRef]

Disclaimer/Publisher's Note: The statements, opinions and data contained in all publications are solely those of the individual author(s) and contributor(s) and not of MDPI and/or the editor(s). MDPI and/or the editor(s) disclaim responsibility for any injury to people or property resulting from any ideas, methods, instructions or products referred to in the content.